A POLAR CORUNDUM OXIDE DISPLAYING WEAK FERROMAGNETISM AT ROOM TEMPERATURE.

Man-Rong Li[1], Umut Adem[1], Sean R.C. McMitchell[1], Zhongling Xu[1], Chris I. Thomas[1], John E. Warren[1], Duong V. Giap[1], Hongjun Niu[1], Xingming Wan[1], Robert G. Palgrave[1], Florian Schiffmann[2], Furio Cora[2], Ben Slater[2], Tim L. Burnett[3], Markys G. Cain[3], Artem M. Abakumov[4], Gustaaf van Tendeloo[4], Michael F. Thomas[5], Matthew J. Rosseinsky[1]*, John B. Claridge[1]*

[1] *Department of Chemistry, University of Liverpool, Liverpool, L69 7ZD,UK*
[2] *Department of Chemistry, University College London, WC1H 0AJ, UK*
[3] *National Physical Laboratory, Hampton Road, Teddington, TW11 0LW, UK*
[4] *EMAT University of Antwerp, Groenenborgerlaan 171, B-2020 Antwerp, Belgium*
[5] *Department of Physics, University of Liverpool, L69 7ZE, UK*

*To whom correspondence should be addressed. E-mail: M.J.Rosseinsky@liverpool.ac.uk, J.B.Claridge@liverpool.ac.uk

The supporting information is organised as follows:

Synthesis of ambient pressure (AP) $ScFeO_3$	S2
Magnetization of the AP Phase $ScFeO_3$ (Bixbyite)	S3
High Pressure (HP) work on non-stoichiometric $ScFeO_3$	S4
Ambient pressure thermal stability of HP $ScFe_{1-x}Cr_xO_3$ (x = 0, 0.03, 0.10)	S5-7
Thin film strain	S8
Calculation of the pseudo-cubic α in thin films of $ScFeO_3$	S9
Convergent Beam Electron Diffraction	S10
Details of calculations	S11-12
Magnetization of $ScFeO_3$ as a function of temperature	S13
P(E) loops	S14
Cole-Cole plots	S15
Overlay of topology and vertical PFM response images in Figure 7	S16
Complete Reference 13 in the manuscript	S17
References	S18

Synthesis of ambient pressure (AP) $ScFeO_3$

Polycrystalline AP $ScFeO_3$ samples were prepared by heating pellets of mixtures of stoichiometric Sc_2O_3 (99.999%, Sigma Aldrich) and Fe_2O_3 (99.999%, Alpha Aesar) powder at 1200 °C 12h in air, and then the product was reheated in air at 1500 °C 12h with intermediate grinding and pelletizing to obtain a pure phase (Fig. S1, the XRD patterns were collected from a PANalytical X'Pert Pro Diffractometer equipped with Co-target and Ge(220) monochromator. All the XRD patterns were collected from this instrument if not specified). The heating and cooling rate was 5 °C/min for both steps. A dense AP $ScFeO_3$ pellet was synthesized under the same heat treatment conditions as a Pulsed Laser Deposition (PLD) target for film growth, with Cold Isostatic Pressing (CIP) at 200 MPa to make a denser pellet before reaction-sintering at 1500 °C 12h as the second step.

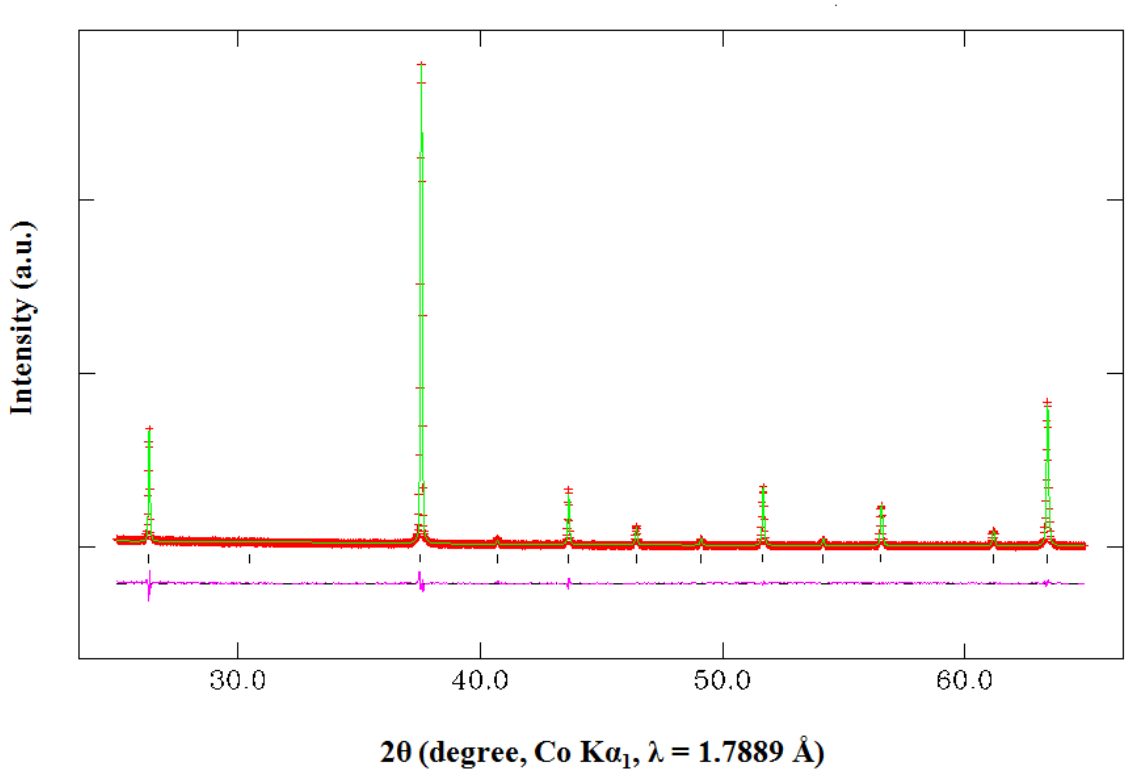

Figure S1| Le Bail fit of AP $ScFeO_3$ phase in bixbyite structure from powder XRD data. Space group, $Ia\bar{3}$, a = 9.6293(1) Å, V = 892.85 Å^3, Rp/Rwp = 6.43/8.03 %, χ^2 = 1.17.

Magnetisation of the AP Phase $ScFeO_3$ (Bixbyite)

Temperature dependence of the magnetic susceptibility at 100 Oe of the AP $ScFeO_3$ with the bixbyite structure is shown in Fig. S2. Zero field cooled (ZFC) and field cooled (FC) measurements diverge below the anomaly around 36 K, suggesting a weak ferromagnetic ordering. A similar ordering temperature was reported in[1].

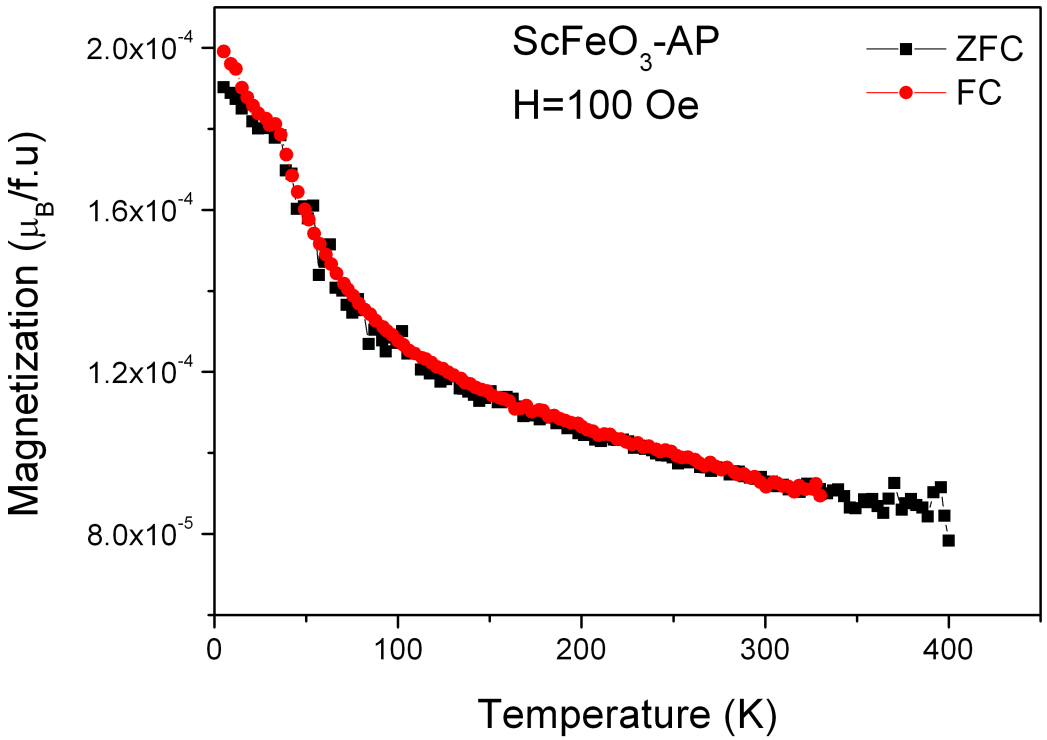

Figure S2| Temperature dependence of ZFC and FC magnetisation of $ScFeO_3$, measured at 100 Oe.

High Pressure (HP) work on non-stoichiometric $ScFeO_3$

Non-stoichiometric $Sc_{1.024}Fe_{0.976}O_3$ (Sc-rich) and $Sc_{0.976}Fe_{1.024}O_3$ (Fe-rich) were also studied to check possible solid solution for HP polar corundum $ScFeO_3$ as described in the text Both Sc- and Fe-rich samples were prepared under the same conditions with $ScFeO_3$ (6 GPa at 1500 °C/5min). HP polar corundum phase and small amounts of Sc_2O_3 and β-Fe_2O_3 (bixbyite structure with space group of $Ia\bar{3}$) impurities were observed in Sc-rich $Sc_{1.05}FeCrO_3$; for Fe-rich $ScFe_{1.05}CrO_3$, HP corundum phase and small amount of β-Fe_2O_3 impurity was observed. The unit cell evolution for both Sc- and Fe-rich cases was examined by Le Bail fitting in GSAS using KCl as internal standard (Space group, $Fm\bar{3}m$, a = 6.293117 Å). It is clearly seen that the Sc-rich material has larger unit cell, and the Fe-rich one a smaller unit cell compared to stoichiometric $ScFeO_3$ (Table S1), which suggests that the solid solution limit is less than 2.4 percent.

Table S1. Unit cell evolution of HP $Sc_{1.024}Fe_{0.976}O_3$ and $Sc_{0.976}Fe_{1.024}O_3$ compared with HP $ScFeO_3$. KCl was used as an internal standard in the refinement.

Composition	a/Å	c/Å	V/Å^3
$Sc_{1.024}Fe_{0.976}O_3$	5.2037(2)	14.0156(4)	328.5(1)
$ScFeO_3$	5.2021(1)	14.0140(2)	328.4(1)
$Sc_{0.976}Fe_{1.024}O_3$	5.2007(1)	13.9916(5)	327.8(1)

AP thermal stability of HP $ScFe_{1-x}Cr_xO_3$ (x = 0, 0.03, 0.10)

Variable temperature powder X-ray diffraction (VT-XRD) analysis for HP $ScFeO_3$

VT-PXRD data for HP $ScFeO_3$ were collected every 10 °C between 100 to 500 °C in a quartz capillary (diameter of 0.3 mm) on instrument I11 (λ = 0.8264 Å) at Diamond Light Source (DLS). As shown in Fig. S3, $ScFeO_3$ starts to decompose at 200 °C accompanied by peak broadening. At 500 °C, decomposition occurred to Sc_2O_3 and α-Fe_2O_3 (starting materials for HP synthesis).

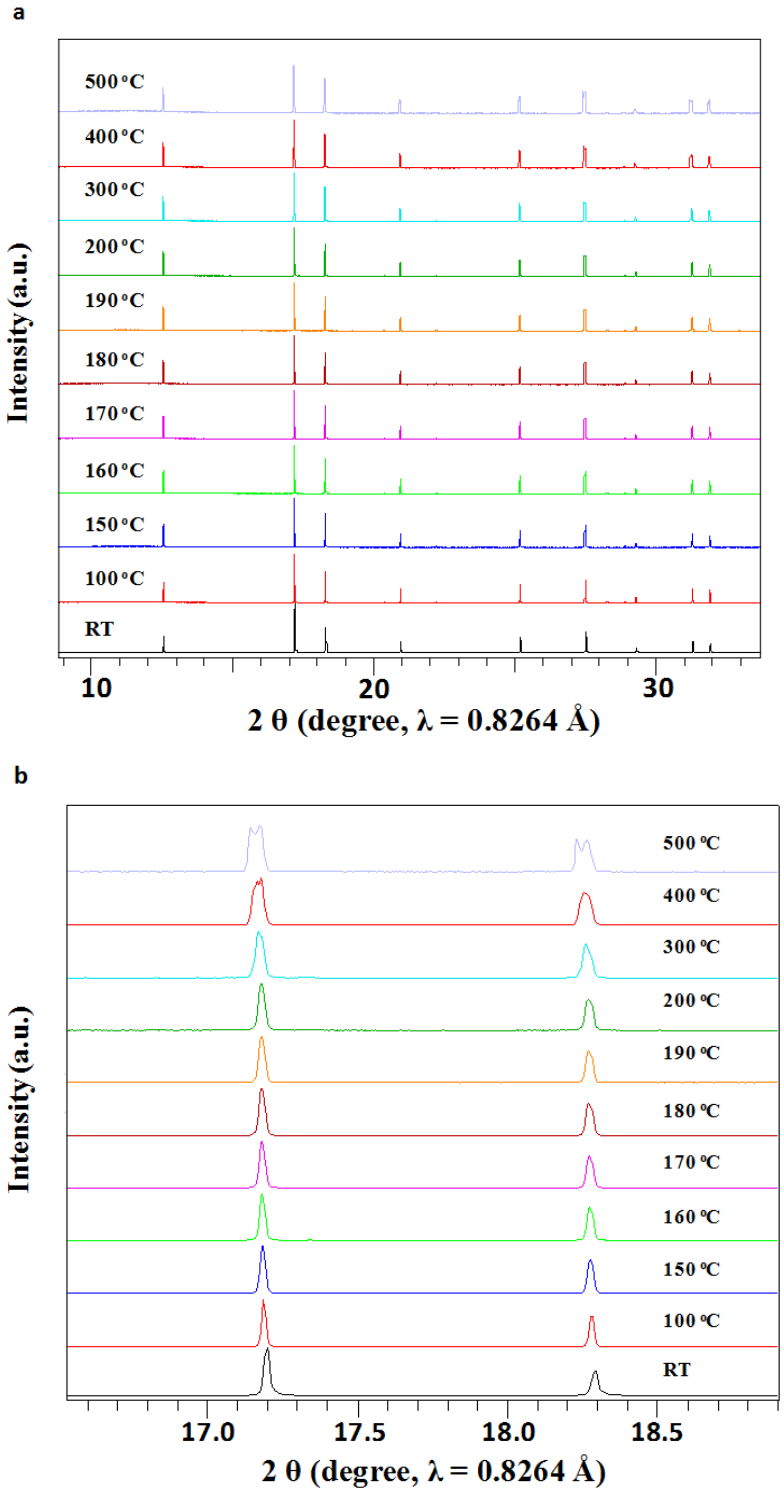

Figure S3| VT-XRD patterns for HP $ScFeO_3$ between 100 and 500 °C. (a) Peak broadening takes place above 200 °C as shown in the enlarged part. (b) At 500 °C, decomposition to Sc_2O_3 and α-Fe_2O_3 occurs.

Thermal annealing of HP $ScFe_{0.97}Cr_{0.03}O_3$ phase

Thermal annealing for as-made $ScFe_{0.97}Cr_{0.03}O_3$ powder was carried out in a tube furnace in air. The sample was heated to temperatures between 400 and 1100 °C (temperature interval of 100 °C) for 6h with heating and cooling rate of 5 °C/min. Diffraction data were collected ex-situ after each thermal treatment. XRD results indicate that $ScFe_{0.97}Cr_{0.03}O_3$ transformed to the AP $ScFeO_3$-type bixbyite structure above 1000 °C (Fig. S4).

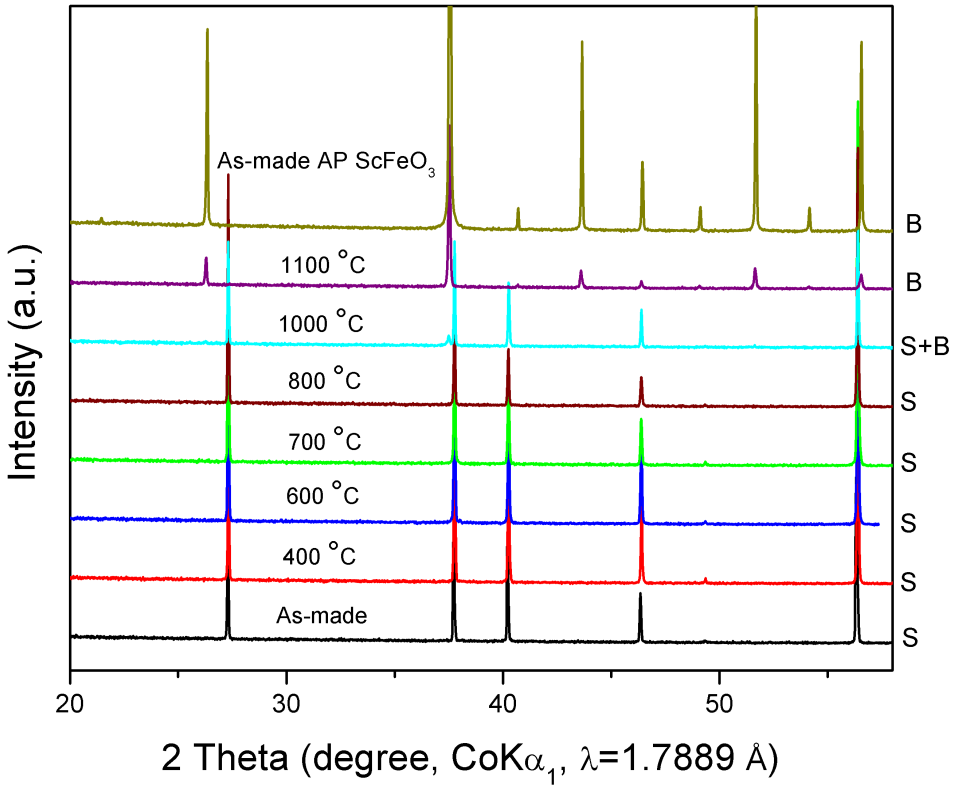

Figure S4| XRD patterns for $ScFe_{0.97}Cr_{0.03}O_3$ after thermal annealing at different temperatures. The phases present at each temperature are marked on the right, where S indicates the HP $ScFeO_3$-type phase and B for the bixbyite structure phase. The XRD pattern of as-made AP $ScFeO_3$ is shown for comparison.

Thermal annealing of HP $ScFe_{0.90}Cr_{0.10}O_3$ phase

Thermal annealing for the as-made $ScFe_{0.9}Cr_{0.1}O_3$ powder was carried out in a tube furnace in air, following the same procedure as for $ScFe_{0.97}Cr_{0.03}O_3$. The sample was annealed at different temperatures (temperature interval of 100 ^oC) for 6h with heating and cooling rate of 5 ^oC/min. As shown in Fig. S5, $ScFe_{0.90}Cr_{0.10}O_3$ is more stable than $ScFe_{0.97}Cr_{0.03}O_3$. The HP phase can be retained up to 1000 ^oC before transforming to bixbyite structure at 1100 ^oC.

In summary, HP $ScFeO_3$ starts to decompose at 200 ^oC, while $ScFe_{0.97}Cr_{0.03}O_3$ and $ScFe_{0.90}Cr_{0.30}O_3$ are stable below 1000 ^oC and 1100 ^oC, respectively, upon heating in air, suggesting that substitution of Fe^{3+} by Cr^{3+} does enhance the AP thermal stability of HP $ScFe_{1-x}Cr_xO_3$.

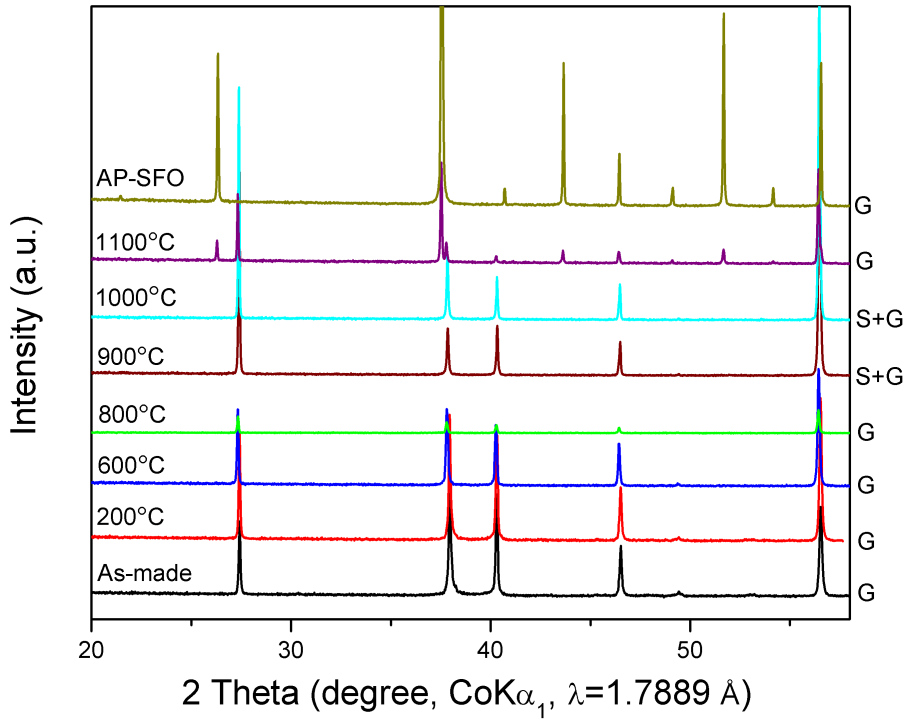

Fig. S5| XRD patterns for $ScFe_{0.90}Cr_{0.10}O_3$ after thermal annealing at different temperatures. The phases present at each temperature are marked on the right, where S is HP $ScFeO_3$-type phase and B is the bixbyite structure phase. The XRD pattern of as-made AP $ScFeO_3$ is shown for comparison.

Thin Film Strain

The reflection high energy electron diffraction (RHEED) pattern for the $SrRuO_3$ buffer layer (Fig. S6a) shows a smooth surface with streaks and strong Kikuchi lines. The lattice rod spacing is consistent with a layer strained to the substrate in-plane lattice parameters. The RHEED pattern taken from the surface shows a three dimensional transmission-like pattern with lattice rod spacing consistent with the doubled perovskite cell of bulk $ScFeO_3$ indicating the film is relaxed.

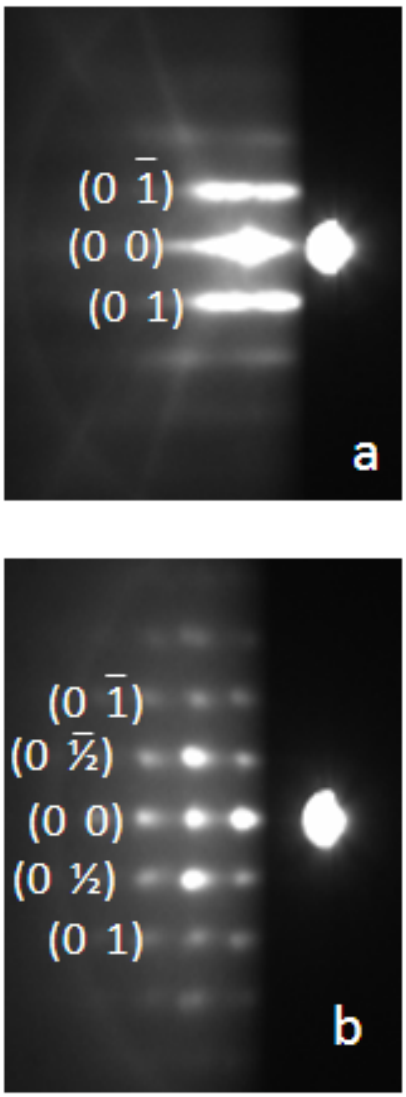

Figure S6| The reflection high energy electron diffraction (RHEED) pattern for the $SrRuO_3$ buffer layer, (a) and for the $ScFeO_3$ film surface indexed to the pseudo-cubic perovskite cell (b) The RHEED pattern for the buffer layer shows a streaky pattern with Kikuchi lines visible indicating an atomically smooth surface. The lattice parameters show it is in tensile strain to the substrate. The film surface shows a structure relaxed to the bulk lattice parameters. The grid-like spotty RHEED pattern indicates a rough surface on an atomic scale.

Calculation of the pseudo-cubic α in thin films of $ScFeO_3$

The d-spacings of two off-axis reflections, $[0\bar{6}6]$ and $[06\ 6]$ were taken from X-ray reciprocal space maps (RSM). These d-spacings were input into the equation for d-spacings of a triclinic cell:

$$\frac{1}{d^2} = \frac{\left[\frac{h^2}{a^2\sin^2\alpha} + \frac{2kl}{bc}(\cos\beta\cos\gamma - \cos\alpha) + \frac{k^2}{b^2\sin^2\beta} + \frac{2hl}{ac}(\cos\alpha\cos\gamma - \cos\beta) + \frac{l^2}{c^2\sin^2\gamma} + \frac{2hk}{ab}(\cos\alpha\cos\beta - \cos\gamma)\right]}{(1 - \cos^2\alpha - \cos^2\beta - \cos^2\gamma + 2\cos\alpha\cos\beta\cos\gamma)}$$

Assuming a = b = 7.81 Å, γ = 90°, and α = β, the two resulting equations were solved to find $\cos^2\alpha$. The assumptions were made in order to satisfy the interfacial boundary conditions of a film strained to the substrate. This process yielded α = 89.2°.

Convergent Beam Electron Diffraction

5 crystallites were checked and 10 CBED patterns were collected along different directions, two of which (from different crystallites and different axes) are shown in Fig. S5 as examples. Fig. S5a is from the $[\bar{4}41]$ axis along which a mirror plane is observed, while the details in discs (hkl) and $(\bar{h}\bar{k}\bar{l})$ disks are different from each other which confirmed the absence of an inversion center for the pattern. Fig. S5b is from a less symmetric axis $[2\bar{\bar{5}}1]$, no symmetry can be identified at all from the CBED pattern. Thus, taking all the TEM data into consideration, a non-centrosymmetric crystal structure with space group R3c can be determined.

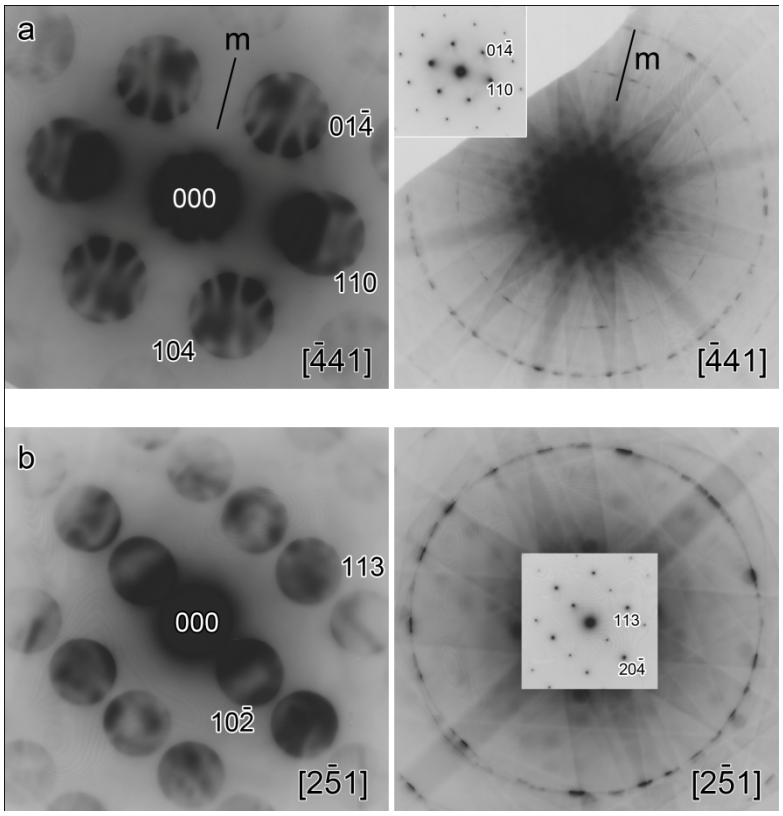

Figure S7| CBED patterns together with their SAED patterns from different crystallites of $ScFeO_3$ along two different axes $[\bar{4}41]$ (a), and $2\bar{\bar{5}}1$ (b), showing the absence of the inversion center of the CBEDs and thus a non-centrosymmetric structure of the material.

DFT calculations

Details of defect energy calculations

In the fully ordered polar corundum crystal, all Fe-O-Fe angles are ~140°; in an isolated antisite defect, additional Fe-O-Fe angles of 90 and 120° are generated. In order to describe simultaneously the energetics of magnetic order and antisite defect formation with an Ising-like model, coupling parameters for each symmetry unique Fe-O-Fe interaction need to be fitted. While in a purely magnetic Ising model it is sufficient to fit a combined coupling constant for FM and AFM states, the introduction of structural defects and magnetic ions in a different environment decouples FM and AFM interactions. Therefore, separate parameters for ferromagnetic and antiferromagnetic couplings have been fitted in this model, according to the following equation:

$$E = E_0 + \sum_{i=1}^{6} N_i J_i$$

With N_i the of iron pairs coupled by the according parameter J_i. The different coupling parameters J_i in the model are: 9.5meV (90° AFM), -9.6meV (120° AFM), -66.7meV (140° AFM) , -11.3meV (90° FM), 52.2meV (120° FM) and -17.9meV (140° FM) . Details about the quality of the fit can be found in Table S3. Parameters have been fitted on the upper set of configurations reported in Table S2, while the lower set of configurations has been used to validate the parameters.

Table S2. Energies obtained for different defects computed with DFT and the extended Ising model. The first column indicates the spin of the ordered polar corundum matrix hosting each defect; S indicates the inversion of one Fe^{3+} spin; C the creation of one antisite defect; (C+S) the creation of an antisite defect accompanied by spin inversion at the Fe ion. The symbol "/" identifies the combination of defects at neighbouring lattice sites.

Configurations used for fitting:				
Matrix	Defect	$E_{def} - E_{ideal}$ [eV]	E (fit) [eV]	ΔE [eV]
AFM	S	0.325	0.293	0.032
AFM	C	0.588	0.585	0.004
AFM	C+S	0.386	0.338	0.049
AFM	(C+S)/(S)	0.765	0.692	0.072
AFM	(C)/(S)	0.839	0.816	0.023
AFM	(C)/(C)	1.052	1.065	-0.013
FM	S	-0.296	-0.293	-0.003
FM	C	0.214	0.230	-0.016
FM	C+S	-0.056	-0.107	0.051
FM	(C+S)/S	-0.122	-0.124	0.002
FM	(C)/(C)	0.336	0.356	-0.020
Configurations used for validation:				
AFM	(C+S)/(C)	0.907	0.870	0.037
AFM	(C+S)/(C+S)	1.314	1.268	0.046
FM	(C)/(S)	0.237	0.264	-0.028
FM	(C+S)/(C)	-0.122	-0.106	-0.016
FM	(C+S)/(C+S)	-0.258	-0.241	-0.017

Polarisation and inversion calculations

The activation energy for polarisation reversal in polar-corundum structured $ScFeO_3$ has been calculated assuming the same mechanism as in the isostructural $LiNbO_3$. There, polarisation reversal occurs via migration of a Li cation through the octahedral face perpendicular to the axis of a cation-cation dimer, to the neighbouring vacant octahedral site. While in $LiNbO_3$ it is uniquely Li that migrates, due to its smaller size and mass compared to Nb; in SFO the Sc and Fe cations are similar, and both are potentially mobile in the polarisation reversal. Hence, activation energies for the migration of both Sc and Fe ions have been evaluated. The displacement of a single ion leads to a very large increase in energy: 1.19 eV for Fe and 1.66 eV for Sc in a FM matrix. Given the high energetic cost of a single-ion migration, we have investigated a concerted mechanism for polarisation reversal, in which all cations of one species displace simultaneously. The activation energies for such concerted mechanism are 0.82 eV for Fe and 0.79 eV for Sc migration (for comparison, the calculated values in $LiNbO_3$, using our computational settings are 0.33 eV for Li and 1.61 eV for Nb). Since these values have been obtained from static calculations and neglect dynamic effects like the breathing motion of the octahedral faces which can assist the transition, these values represent an upper bound for the barriers.

Calculated positional parameters and bond lengths in fully ordered $ScFeO_3$

The calculated atomic coordinates and bond lengths are given in Tables S3 and S4, respectively.

Table S3. Calculated (DFT) atomic coordinates in fully ordered $ScFeO_3$.

Atom	Occupancy	x/a	y/b	z/c
Sc	1	0	0	0.27389
Fe	1	0	0	0.6038
O	1	-0.37626	-0.35247	0.33302

Table S4. Selection of calculated bond-lengths in fully ordered $ScFeO_3$.

Bonds	Bond Length (Å)
Fe-O1 (3)	1.9533
Fe-O2 (3)	2.1524
Sc-O1 (3)	2.0735
Sc-O2 (3)	2.1674

Magnetization of $ScFeO_3$ as a function of temperature

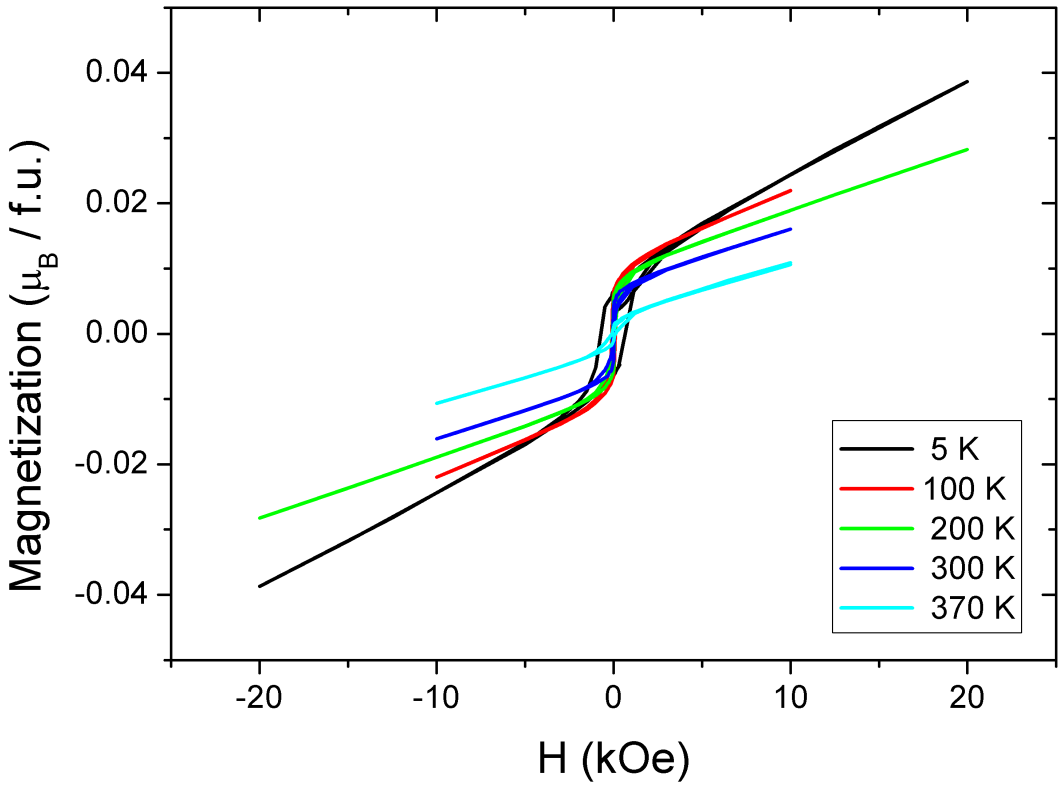

Figure S8| M(H) curves of polar corundum $ScFeO_3$ at different temperatures. Black, red , green, blue and cyan correspond to datasets collected at 5, 100, 200, 300 and 370 K, respectively.

P(E) loops

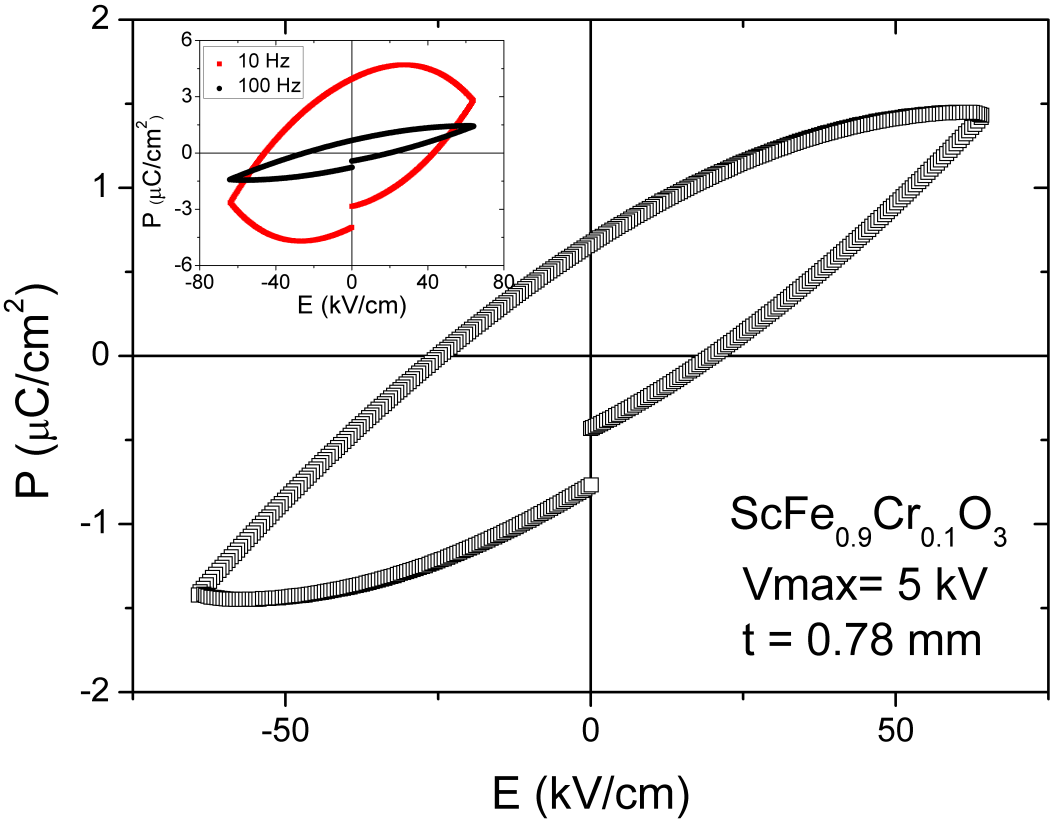

Figure S9| P(E) loops for $ScFe_{0.9}Cr_{0.1}O_3$ under 5 kV at 100 Hz. In order to show the effect of frequency on the measured loops, 10 Hz and 100 Hz data are plotted together in the inset. As the frequency is increased, the loops close-up, indicating the removal of the influence of extrinsic charge carriers. P(E) loops are consistent with leakage or sub-switching field polar behavior. For an example of sub-switching behavior please see[2]

Cole-Cole plots

Cole-Cole plots for for $ScFe_{1-x}Cr_xO_3$ (x = 0 and 0.1) corresponding to the dielectric data in Figure 8 of the manuscript are shown below in Figure S10. Due to large dielectric loss, the Cole-Cole plot for the $ScFeO_3$ shown in Figure S10(a) is fully dominated by the conduction tail. For the case of $ScFe_{0.9}Cr_{0.1}O_3$, the conduction tail also dominates the Cole-Cole response and only in the high frequency regime, there is some levelling off (shown in the inset of Figure S10(b)). This level-off behaviour might be associated to the intrinsic Debye-like relaxation of the material.

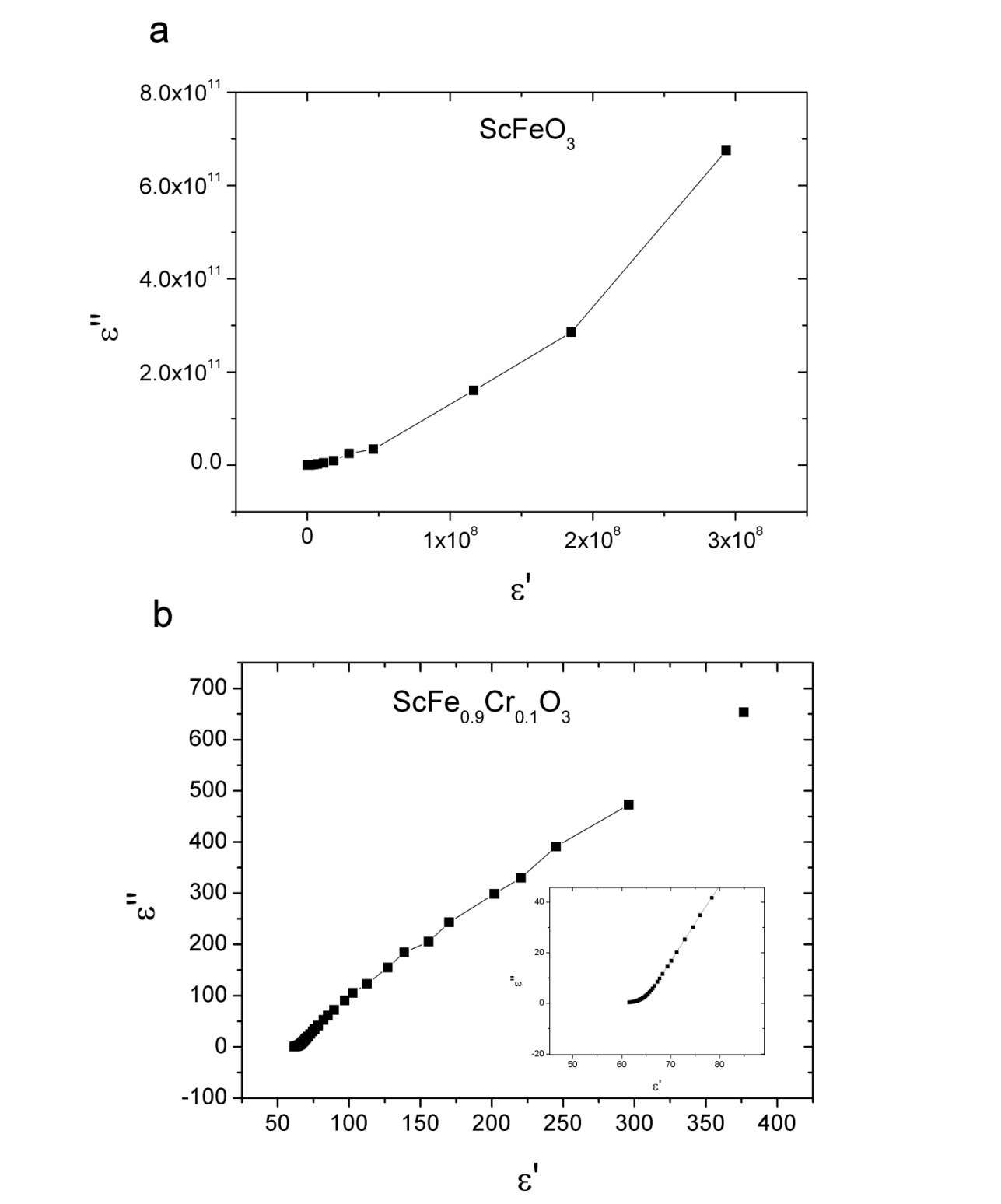

Figure S10| Cole-Cole plots of **(a)** $ScFeO_3$ **(b)** $ScFe_{0.9}Cr_{0.1}O_3$. The inset in b shows a zoomed-in version of the high frequency data.

Overlay of topology and vertical PFM response images in Figure 7

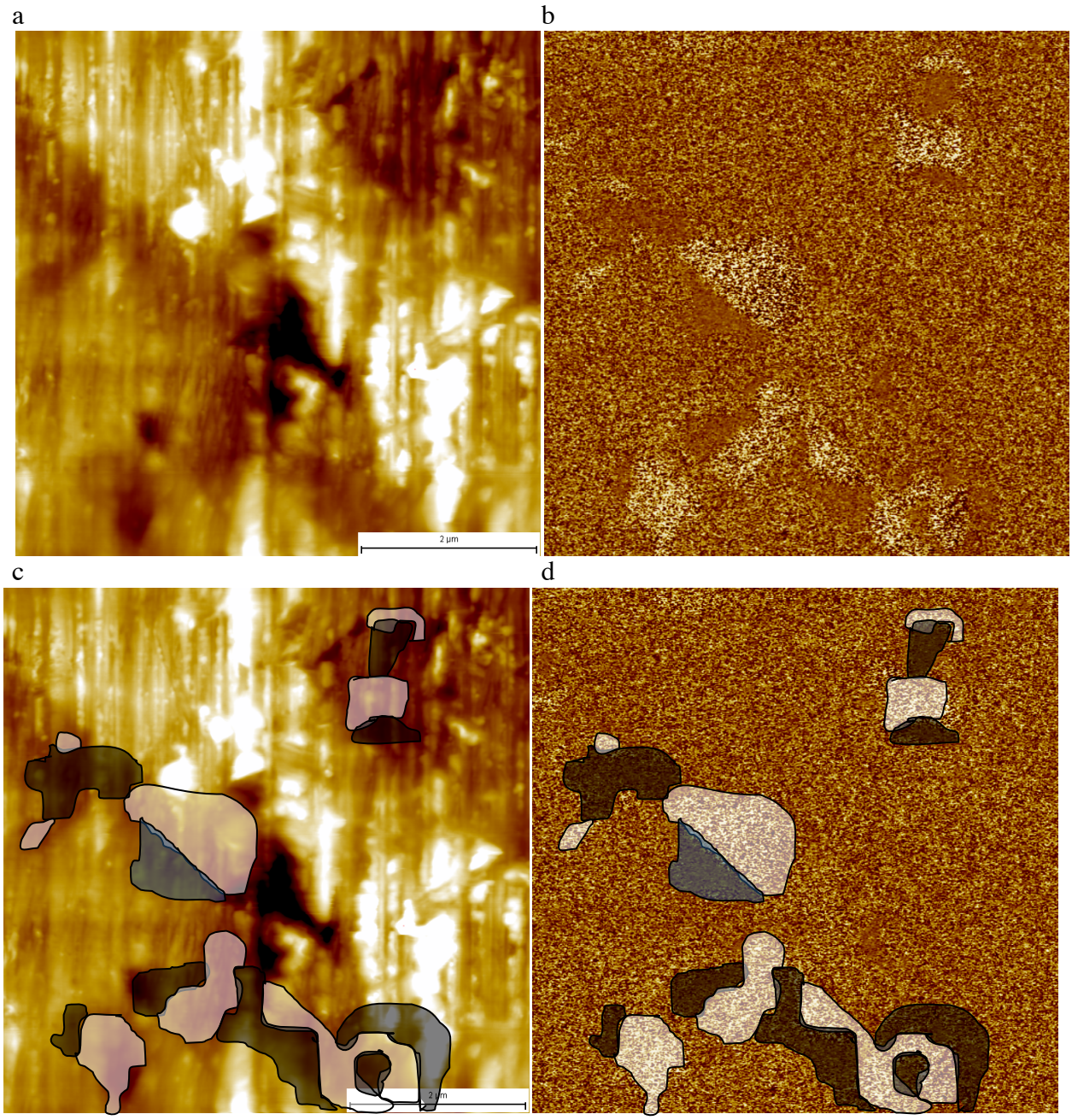

Figure S11| Piezoresponse force microscopy images of $ScFeO_3$ **(a)** Topography **(b)** Vertical PFM phase response as given in Figure 7 (a) and (b). In (c) and (d) the same figures in (a) and (b) are duplicated respectively; with contrast images added on Vertical PFM response in (d) being overlaid on (c). The superposition of the figures in (c) reveals that there is no correlation present between the topology and vertical PFM response for the two domains shown here.

Complete Reference 13 in the manuscript

(13) Lee, J. H.; Fang, L.; Vlahos, E.; Ke, X.; Jung, Y. W.; Kourkoutis, L. F.; Kim, J. W.; Ryan, P. J.; Heeg, T.; Roeckerath, M.; Goian, V.; Bernhagen, M.; Uecker, R.; Hammel, P. C.; Rabe, K. M.; Kamba, S.; Schubert, J.; Freeland, J. W.; Muller, D. A.; Fennie, C. J.; Schiffer, P.; Gopalan, V.; Johnston-Halperin, E.; Schlom, D. G. *Nature* **2010**, *466*, 954.

References

(1) Breard, Y.; Fjellvaag, H.; Hauback, B. *Solid State Communications* **2011**, *151*, 223.
(2) Damjanovic, D. in *Science of hysteresis*; Bertotti, G., Mayergoyz, I., Eds.; Academic Press: 2006.